# Emergent Wave Conversion as a Precursor to Shear Crack Initiation

**Article** *in* Geophysical Research Letters · September 2018

DOI: 10.1029/2018GL078622



**3 authors**, including:

Anahita Modiriasari
Purdue University
**10** PUBLICATIONS **10** CITATIONS

SEE PROFILE

Geophysical Research Letters

RESEARCH LETTER
10.1029/2018GL078622

**Key Points:**
- Emergent wave conversion occurs at the onset of shear crack formation
- Elastic wave conversions are attributed to an array of similarly oriented microcracks that form and dilate under shear stress

**Correspondence to:**
A. Modiriasari,
amodiria@purdue.edu

**Citation:**
Modiriasari, A., Pyrak-Nolte, L. J., & Bobet, A. (2018). Emergent wave conversion as a precursor to shear crack initiation. *Geophysical Research Letters*, *45*. https://doi.org/10.1029/2018GL078622

Received 3 MAY 2018
Accepted 25 AUG 2018
Accepted article online 4 SEP 2018



# Emergent Wave Conversion as a Precursor to Shear Crack Initiation

**Anahita Modiriasari[1], Laura J. Pyrak-Nolte[1,2,3], and Antonio Bobet[1]**

[1]Lyles School of Civil Engineering, Purdue University, West Lafayette, IN, USA, [2]Department of Physics and Astronomy, Purdue University, West Lafayette, IN, USA, [3]Department of Earth, Atmospheric, and Planetary Sciences, Purdue University, West Lafayette, IN, USA

**Abstract** Geophysical assessments of subsurface instability rely on a link between physical failure mechanisms and a geophysical measurement. Here a laboratory study demonstrates the emergence of a converted phase at the damage onset in limestone prior to failure from shear crack formation. Shear (*S*) to compressional (*P*) wave conversions arise from the presence of an array of disconnected microcracks and occur prior to the crack initiation detection from surface displacement measurements. The converted waves increase in amplitude with shear crack propagation until crack coalescence. The inception of the *S* to *P* wave converted phase supports the use of elastic wave conversions as an active diagnostic tool to detect the initiation and propagation of shear cracks.

**Plain Language Summary** Crack initiation, propagation, and coalescence in the Earth's subsurface is caused by natural and engineering processes. Understanding a link between physical failure mechanisms and a geophysical measurement to identify precursors to failure is significantly important. The authors has identified precursors associated with crack formation, distinct changes in the compressional (*P*) and shear (*S*) wave amplitudes with stress prior to the initiation of tensile cracks. However, shear crack initiation could not be detected from compressional or shear amplitudes. Here a laboratory study demonstrates that *S* to *P* converted waves arise at the onset of shear damage in rock as a precursory signature of shear crack formation. These converted phases, even at normal incidence, are attributed to the formation of an array of oriented microcracks that dilate under shear stress. The results present an intriguing potential geophysical signal for monitoring damage evolution in the subsurface.

## 1. Introduction

Natural and engineered processes in the Earth's subsurface initiate, propagate, and coalesce cracks. Identification of precursors to failure requires a fundamental understanding of the effect of fracture initiation and propagation, as well as slip along fractures on the transmission and reflection of seismic waves, and how these effects scale with the signal wavelength. Several precursors to slip along fractures and other mechanical discontinuities have been identified in previous studies that include nonmonotonic changes in *P* and *S* wave amplitudes (Chen et al., 1993; Hedayat et al., 2014; Nagata et al., 2008) and distinct maxima in transmitted and minima in reflected low-amplitude signals prior to slip (Rouet-Leduc et al., 2017). Reductions in *P* wave velocity during accelerated fault creep (Scuderi et al., 2016) as well as incipient *P*-to-*S* wave conversions during shearing along a fracture (Nakagawa et al., 2000) are other examples of slip precursors. Other research has identified precursors associated with crack formation, for example, the emergence of compressional mode fracture interface waves during tensile failure (Pyrak-Nolte & Roy, 2000) and distinct changes in the *P* and *S* wave amplitudes with stress prior to the tensile cracks initiation (Modiriasari et al., 2017). While tensile crack initiation resulted in the aforementioned precursors, Modiriasari et al. (2017) found that shear crack initiation could not be detected from compressional or shear amplitudes. In this paper, we demonstrate that *S*-to-*P* converted waves arise at the shear damage onset in rock and provide precursory signatures of shear crack formation. These converted phases, which occur even at normal incidence to a shear crack growth zone, are a function of the local-induced microcrack orientation prior to coalescence, the stiffness of the evolving damage zone, and the signal frequency.

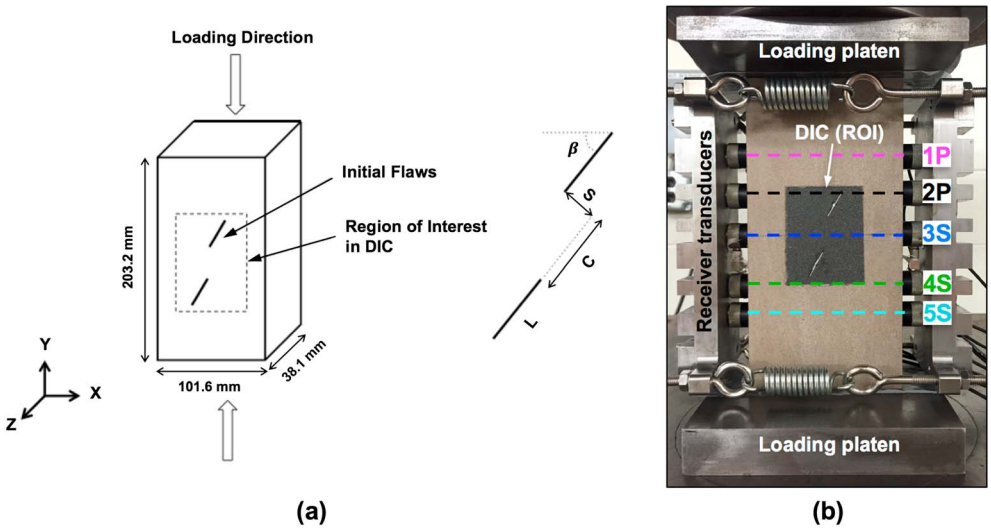


**Figure 1.** Test geometry. (a) Flaw geometry. *L*: flaw length, *S*: normal distance between the flaws, *C*: continuity, and $\beta$: inclination angle with respect to the *x* axis. (b) Setup for seismic wave monitoring. DIC = digital image correlation; ROI = region of interest.

## 2. Experimental Methods

The initiation and propagation of shear cracks in rock can be controlled in the laboratory by designing samples with specific preexisting cracks or flaws (Bobet & Einstein, 1998; Park & Bobet, 2010). In this study, prismatic specimens of Indiana limestone with two parallel flaws were prepared to determine the seismic signatures of shear crack initiation and growth under uniaxial compression (Figure 1). The dimensions and average physical properties of the samples are listed in Table 1. The samples exhibited seismic anisotropy that corresponded to planar bedding in the samples (parallel to *XY* plane in Figure 1a). The *P* and *S* wave velocities listed in Table 1 are averages measured across different dimensions of specimens.

The two flaws were cut through the specimen thickness in the *z* direction using a scroll saw (Figure 1a). The flaws aperture was ~1 mm. The flaws geometry is defined by $SC\beta$, where *S* denotes the normal distance between the flaws, *C* the continuity, and $\beta$ the inclination angle relative to the *x* axis (Figure 1a). The measurements are given in multiples of $a$ = 9.525 mm, which is one half of the flaw length (*L*). Experiments were performed on samples with a two-flaw geometry with $S$ = 1$a$=9.525 mm, $C$ = 2$a$=19.05 mm, and $\beta$= 60°. This geometry was selected because flaw coalescence occurs through shear cracks (Bobet & Einstein, 1998; Park & Bobet, 2010). Ten experiments were performed for this geometry to test the repeatability of the results. Only the results of one representative specimen are discussed here.

Samples were loaded in uniaxial compression using an Instron loading machine with a constant displacement rate of 0.04 mm/min. The loading direction was parallel to the *Y* direction (Figure 1a). A 0.05-mm-thick Teflon film coated with a thin layer of petroleum jelly was placed in contact with the loading platens to minimize the friction between the rock and platen and to reduce the potential stress concentration on a specimen. A sampling rate of 1 Hz was used to record the applied load and displacement in the *Y* direction, from initial loading until sample failure.

Concurrently, ultrasonic transducers were used to measure transmitted and reflected *P* and *S* waves during shear crack evolution. Source and receiver arrays (each containing five piezoelectric transducers) were housed in steel plates placed on the specimen sides (Figure 1b). The receiver transducers (on the left side of the sample) recorded transmitted signals generated by the source transducers (on the right side of the sample). Reflected waves were both generated and recorded with the source transducers. The steel plates

**Table 1**
*Dimensions and Physical and Mechanical Properties of Indiana Limestone Specimens*

| Dimension/property | Indiana limestone |
|---|---|
| *X*, *Y*, *Z* dimensions (mm) | 101.6, 203.2, 38.1 |
| Density (kg/m$^3$) | 2,326 |
| Young's modulus (MPa) | 7,415 |
| Unconfined compressive strength (MPa) | 47 |
| Compressional wave velocity (m/s) | 4,380 |
| Shear wave velocity (m/s) | 2,570 |

were held in place with four springs under 70-kPa tension. The ultrasonic transducers (Panametrics V103RM *P* wave and V153RM *S* wave transducers) had a central frequency of 1 MHz. Square wave pulses were generated with an amplitude of 400 V and a repetition rate of 5 kHz. Transducer 3S (Figure 1b) probed the region of shear crack formation between the flaws. In addition, crack coalescence occurred through the connection of the internal shear cracks of the two flaws in the ligament area. The 3S transducer pair was polarized vertically, parallel to the *Y* direction in Figure 1a. In addition to transducer pair 3S, two transducer pairs, 1P and 5S, were used to record waves passing through the intact material for reference signals. One transducer pair, 2P, was aligned with the external tip of the top flaw to monitor tensile crack initiation and propagation in the rock. The other transducers pair, 4S, was used to monitor the propagation of the tensile crack originating from the external tip of the bottom flaw.

Before the experiment was conducted, a layer of oven-baked honey was applied to establish good coupling between the sensors and the specimen. The honey was baked at 90 °C for ~90 min until 5% of the moisture evaporated. After monitoring the transducer arrays, the sample was subjected to a stress of 2 MPa for 4 hr to enable coupling equilibration and to stabilize the signals (i.e., constant amplitudes). Then the specimens were loaded in uniaxial compression until failure. Signals were generated, and full waveforms (100-μs window) were recorded for the entire array every second using a Labview-controlled data acquisition system.

Crack initiation and propagation were also monitored on the specimen surface using two-dimensional (2-D) digital image correlation (2-D-DIC) to measure the surface displacements in the region of interest (ROI, gray square in Figure 1b). A Grasshopper (Point Gray) CCD camera with 2,248 ×2,048 pixels in combination with a Fujinon lens (Model HF50SA-1) with a focal length of 50 mm was used to capture digital images during the experiment. DIC images were taken at a 2-frames/s rate. After the experiment, the digital images were analyzed using the Vic-2-D software (licensed by Correlated Solutions). In DIC analysis, digital images acquired during deformation are compared to a digital image from before deformation (reference image) to measure the full-field displacements and strains in the ROI on the specimen surface (Chu et al., 1985; Pan et al., 2009; Sutton et al., 2009). The ROI has a random speckle pattern with a random gray value intensity distribution. During the DIC analysis, the ROI is divided into small subsets with a uniform grid. The advantage of choosing a subset rather than a single point is the unique arrangement of grayscale intensity values in the subset matrix. The displacements are measured using a correlation algorithm to compare the deformed subsets with the reference subset (Pan et al., 2009). Optimal matching between the deformed and reference subsets is found when the correlation between the two subsets reaches an extremum. The displacement is calculated as the difference between the new position of the deformed subset (coordinate of the extremum position) and the center of the reference subset (Hedayat et al., 2014; Lin & Labuz, 2013; Pan et al., 2009; Sutton et al., 2009). The imaging system had a spatial resolution of 28 μm/pixel and a displacement resolution of ~1 μm.

## 3. Results and Discussion

Compressional and shear waves were recorded to determine if precursory signatures exist during the shear cracks formation prior to crack coalescence and failure. Figures 2b–2g show the evolution of a shear crack obtained from the interpretation of the DIC images in a specimen with two flaws and geometry 1a2a60. A crack was identified when there was a difference in horizontal displacement of 5 μm between two points. This threshold value was larger than the noise in the DIC data and provided enough resolution to determine the location of any new crack tip. The initiation of a new shear crack at the internal tips of the two flaws was observed at a load of 88 kN based on the DIC measurements (Figure 2c). As the load increased, shear cracks continued to grow until coalescence occurred at ~92 kN (Figure 2e). The DIC results show that the shear crack propagation path between the two flaws was roughly perpendicular to the incident waves from transducer 3S (Figure 1b).

Normalized amplitudes of transmitted *S* waves (blue circles), converted *S* to *P* waves (purple triangles), and reflected *S* waves (green squares) from transducer 3S, as a function of compression load, are shown in Figure 2a (the converted and reflected wave amplitudes are only plotted after their emergence in the waveforms). The amplitudes were extracted from wavelet analysis (Combes et al., 1989; Nolte et al., 2000; Polikar, 1999; Sheng, 1995) for a 440-kHz frequency and were normalized with respect to the initial value of the transmitted shear wave amplitude.

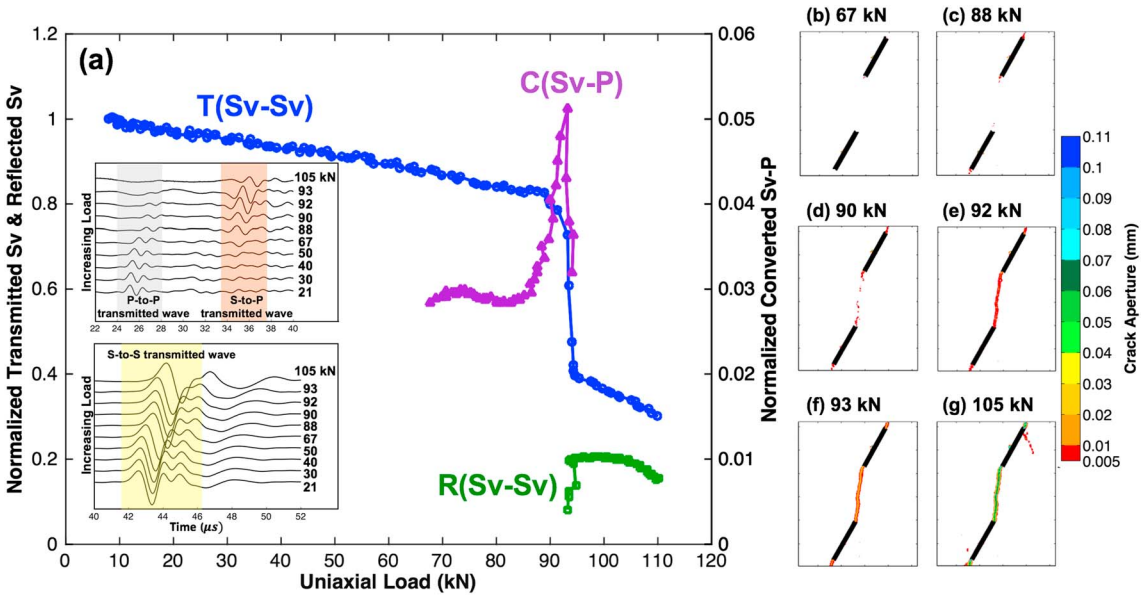


**Figure 2.** (a–g) Specimen 1a2a60. Normalized amplitude of transmitted *T* (*Sv-Sv*), blue circles; reflected *R* (*Sv-Sv*), green squares; and converted *C* (*Sv-P*), purple triangles, signals from transducer 3S (see Figure 1b for transducer location) with uniaxial compression; the insets show the received transmitted *P* and converted *S*-to-*P* and transmitted *S* wave waveforms from transducer 3S with uniaxial compression (*S* wave transducers generate small-amplitude *P* waves in addition to *S* waves); cracks initiation and propagation at the flaw tips with load, obtained from digital image correlation results.

A steady decrease in the normalized amplitude of the transmitted shear wave occurred until ~90 kN, which is associated with the microcracks opening inside the intact rock. The first clear seismic signature of the damage from the transmitted *S* wave initiated at ~90 kN. Significant changes in the gradient of the transmitted *Sv* wave amplitude only occurred at a load of ~92 kN, which coincides with crack coalescence. This observation confirms previous findings (Modiriasari et al., 2017) that show that shear crack initiation and growth are not detected by transmitted waves until significant deformation has occurred.

However, from the full waveform analysis, an emergent mode (*S* to *P* in insets in Figure 2a) is observed as the load increased. The transmitted *P* wave (gray region in Figure 2a inset) arrives at ~25 μs (*S* wave transducers generate small amplitude *P* waves in addition to *S* waves). The transmitted *S* wave (yellow region in Figure 2a inset) arrives after 40 μs. A third wave emerges at a load of ~67 kN (17.3 MPa) with an arrival time of 34.7 μs. The arrival time of this emergent mode is consistent with the arrival time of a converted *S*-to-*P* wave (orange region in Figure 2a inset) for the shear crack location obtained from the DIC images (Figures 2b–2g). The *S*-to-*P* conversions emerged at ~76% of the load at which shear crack initiation was detected from the DIC imaging.

The emergence of an *S*-to-*P* converted phase for a wave that is normally incident to a fracture has been experimentally observed during shearing along a preexisting synthetic fracture (Nakagawa et al., 2000). Nakagawa et al. (2000) predicted the emergence of converted waves from the extension of the displacement discontinuity theory (Pyrak-Nolte et al., 1990; Schoenberg, 1980, 1983) to include cross-coupling fracture-specific stiffnesses. They showed that when a shear crack dilates, normal and shear displacements occur caused by shear and normal stresses on the crack plane, respectively. Under shearing, an array of similarly oriented microcracks is formed that results in cross-coupling compliances greater than zero. This results in the emergence of *S*-to-*P* wave conversions even at normal incidence and affects energy partitioning among the transmitted, reflected, and converted wave phases.

The experimental observations in Figure 2a show that wave conversion (*S* to *P*) occurs prior to the generation of a reflected wave from damage inside the rock. From the data, the *S*-to-*P* converted phase increases in amplitude with increasing load until close to failure (up to 92 kN). At failure, the array of oriented microcracks coalescences and forms an open fracture that no longer exhibits cross coupling.

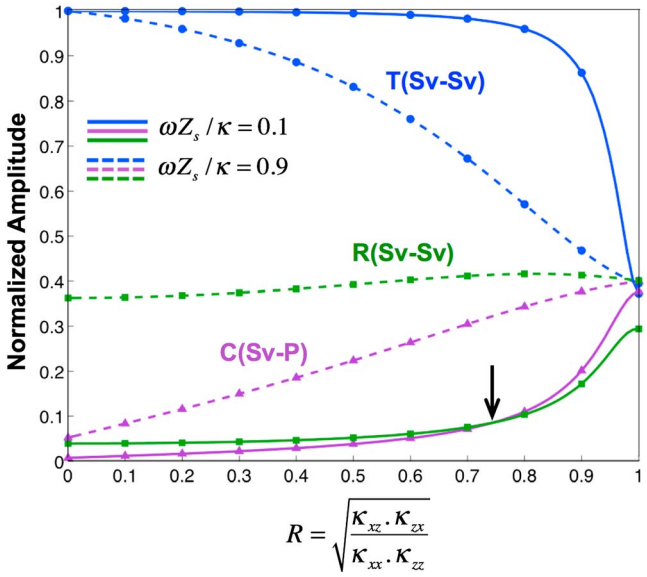


**Figure 3.** Transmission *T* (*Sv-Sv*), conversion *C* (*Sv-P*), and reflection *R* (*Sv-Sv*), coefficients with the ratio *R*, for a *S* wave incident on a fracture at ~10°, and normalized frequencies $\omega Z_s/\kappa$= 0.1 (solid lines) and 0.9 (dashed line). The black arrow shows the crossover point between the converted and reflected amplitudes.

The extended displacement discontinuity theory was used to analyze the changes in the wave amplitude (Figure 2a) during shear crack initiation. Nakagawa et al. (2000) showed theoretically that the transmitted, reflected, and converted wave coefficients are a function of fracture stiffness (normal, shear, and cross-coupling stiffnesses), normalized frequency $\omega Z/\kappa$ (where $\omega$ is the wave angular frequency, $Z$ is the seismic impedance defined as the product of the density and phase velocity of the fracture half-spaces, and $\kappa$ is the fracture stiffness) and the angle of incidence. The normal specific fracture stiffness ($\kappa_{zz}$) is the ratio between the normal stress applied to the discontinuity and the excess in normal displacement caused by the discontinuity presence (Cook, 1992; Pyrak-Nolte, 2018). Analogously, shear-specific fracture stiffness ($\kappa_{xx}$) is the ratio between the shear stress acting on the fracture and the induced excess tangential displacement. The cross-coupling stiffnesses ($\kappa_{xz}$ or $\kappa_{zx}$) are defined, respectively, as the ratios between the tangential and normal stresses applied to the fracture and the normal and tangential displacements produced. In the extended theory, the cross-coupling stiffness is a function of the microcracks orientation. Nakagawa et al. (2000) defined the relative magnitude of the fracture coupling stiffness as

$$R = \sqrt{\frac{\kappa_{xz}.\kappa_{zx}}{\kappa_{xx}.\kappa_{zz}}} \quad (1)$$

*R* ranges from 0 (corresponding to 0° inclination) to 1 (corresponding to crack inclinations greater than ~60°). The ratio *R* depends on the fracture geometry and does not change if the overall size/scale of the crack array only changes. This means that for an array of similarly oriented cracks, as the number or length of individual cracks increases, all the components of the fracture stiffness matrix decrease proportionally such that the relative coupling stiffness *R* does not change. However, the ratio *R* gradually decreases to a small value since the fracture geometry changes as the dominant microcrack orientation is lost through microcrack coalescence.

The amplitudes of the transmitted (*Sv-Sv*), converted (*Sv-P*), and reflected (*Sv-Sv*) waves for an incident *S* wave, as a function of the ratio *R*, are shown in Figure 3. The transmitted (blue lines), converted (purple lines), and reflected (green lines) amplitudes are normalized with respect to the transmitted *Sv* wave amplitude at zero normalized frequency (infinite fracture specific stiffness, i.e., intact rock with no fracture is present). The angle of incidence is assumed to be ~10° based on the fracture orientation in the DIC (Figures 2b–2g). Material properties used include the following: density $\rho$= 2,326 kg/m$^3$, *S* wave velocity $V_s$=2,352 m/s, and *P* wave velocity $V_p$=4,000 m/s which are the material properties of the specimen shown in Figure 2a. The analysis was performed for a 440-kHz frequency. Normal and shear fracture stiffnesses are assumed to be equal (i.e., $\kappa_{xx} = \kappa_{zz} = \kappa$). The coefficients are shown for two different normalized frequencies of 0.1 (solid line) and 0.9 (dashed line) that were obtained by appropriately adjusting the stiffnesses. For a *S* wave incident at 10° to the fracture, the converted and reflected wave amplitudes (green and purple lines) increase with *R* (Figure 3). In contrast, the transmitted wave amplitudes decrease (blue lines).

The crossover point between the converted and reflected amplitudes occurs at a normalized frequency smaller than ~0.9 (e.g., black arrow at *R* ~0.75 in the figure is the crossover point for a normalized frequency of 0.1). After the crossover point, the converted wave amplitude is larger than the reflected wave, which is consistent with the emergence of wave conversions before the generation of reflected waves at the shear crack onset in the experiments. In Nakagawa et al. (2000), these values of *R* corresponded to an array of oriented cracks with a minimum inclination angle of ~40°. This observation seems to support the hypothesis that before the shear crack is observed on the specimen surface, a network of oriented microcracks with a minimum inclination angle ~40° forms inside the rock that causes the wave conversions from *S* to *P*. For normalized frequencies $<$ ~0.9 and $R >$ ~0.75, the cross-coupling stiffnesses ($\kappa_{xz}$ or $\kappa_{zx}$) of the shear crack in the specimen are estimated to be greater than ~17 TPa/m.

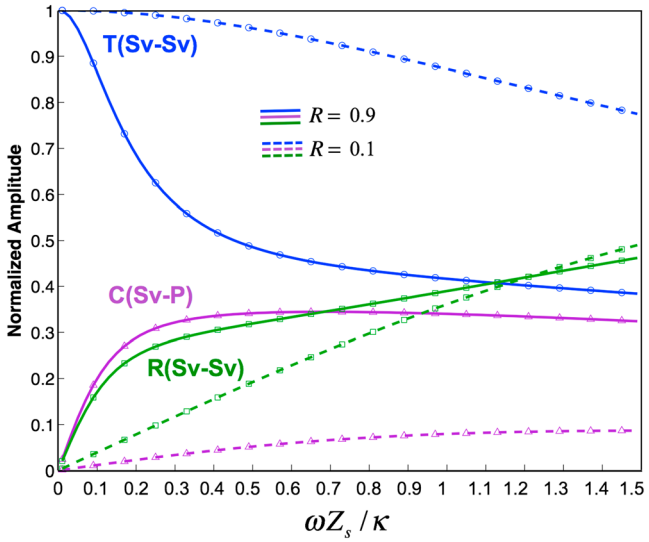


**Figure 4.** Transmission *T* (*Sv-Sv*), conversion *C* (*Sv-P*), and reflection *R* (*Sv-Sv*) coefficients with normalized frequency for a *S* wave incident on a fracture at 10° and constant ratio *R* (0.1 or 0.9).

Figure 2a shows that a distinct maximum in the normalized converted wave amplitude occurred at crack coalescence (92 kN). After 92 kN, the inclined microcracks coalesced to form an open crack (Figure 2e). The converted wave amplitude decreased as the crack aperture increased to greater than 10 μm and then with continued loading, loss of contact between the two shear crack surfaces occurred. At the same load (92–93 kN), reflected waves from the coalesced cracks were detected. The minimum in the transmitted and converted wave amplitudes corresponded to the maximum of the normalized amplitude of reflected waves. After the two shear crack surfaces separated, most of the wave energy was reflected off the shear crack surfaces.

These observations are supported by the theory. Figure 4 shows the normalized amplitude of the transmitted, reflected, and converted phases with respect to the normalized frequency, for an incident angle of 10° and a constant cross-coupling ratio $R$= 0.1 or 0.9 (only two values of $R$ are selected and shown for clarity).

For a given $R$, the amplitude of the transmitted and reflected waves monotonically decreases and increases, respectively, as the fracture propagates and the fracture stiffness decreases (normalized frequency increases). The converted wave amplitudes, however, first increase and then decrease (Figure 4) and have a peak value at a normalized frequency ($\omega Z_s/\kappa$) between 0.1 and 1, when $R$ is greater than 0.75. As discussed, the fracture geometry changes as the cracks coalescence and the ratio $R$ decreases. The theory shows that as $R$ decreases to 0.1 (i.e., crack coalescence), the reflected wave amplitudes are greater than the converted wave amplitudes. Thus, the decrease in *S-P* converted wave amplitude and the increase in the reflected wave amplitude observed in these experiments, as coalescence was approached, are consistent with changes in the microcrack geometry caused by microcrack coalescence.

## 4. Conclusions

A key challenge in monitoring subsurface reservoirs is the identification of geophysical precursors for a rock system transitioning from stable to unstable behavior because of the nucleation and growth of shear and tensile cracks in response to changes in pressure and stress. From this laboratory study, precursors to shear crack formation were manifested as *S*-to-*P* converted waves caused by damage that generated a two-dimensional array of oriented microcracks between flaws. These emergent converted phases exist even for waves that are normally incident on an evolving fracture and are observed at loads as low as 66% of the ultimate failure load. These results present an intriguing potential geophysical signal for monitoring damage evolution in the subsurface.

An important question is how well the observed precursors can be extended to borehole or crosshole frequencies (e.g., 100–20 kHz). The extended displacement discontinuity theory for *P-S*/*S-P* conversions has a characteristic frequency that determines the range of fracture specific stiffness that can be detected for a selected frequency. In the field, the induced damage between preexisting cracks on the 1-mm to 1-cm scale in the laboratory would not be observed at field frequencies. However, a plane of damage between two preexisting joints (1–10 m) might be observable. The extent of the required damage zone (i.e., oriented cracking) would need to scale with the signal wavelength.

**Acknowledgments**
This research has been supported by the National Science Foundation, Geomechanics and Geotechnical Systems Program, under grant CMMI-1162082. This work also received substantial help from Seiji Nakagawa at Lawrence Berkeley National Lab. The authors are grateful for these supports. Data are stored in the Purdue University data repository (PURR) https://purr.purdue.edu/projects/geophysicalfrac.

## References

Bobet, A., & Einstein, H. H. (1998). Fracture coalescence in rock-type materials under uniaxial and biaxial compression. *International Journal of Rock Mechanics and Mining Sciences*, *35*(7), 863–888. https://doi.org/10.1016/S0148-9062(98)00005-9

Chen, Q.-Y., Lovell, C. W., Haley, G. M., & Pyrak-Nolte, L. J. (1993). Variation of shear-wave amplitude during frictional sliding. *International Journal of Rock Mechanics and Mining Sciences*, *30*(7), 779–784. https://doi.org/10.1016/0148-9062(93)90022-6

Chu, T. C., Ranson, W. F., & Sutton, M. A. (1985). Applications of digital-image-correlation techniques to experimental mechanics. *Experimental Mechanics*, *25*(3), 232–244. https://doi.org/10.1007/BF02325092

Combes, J., Grossmann, A., & Tchamitchian, P. (1989). Wavelets: Time-frequency methods and phase space. *The Journal of the Acoustical Society of America*, *89*(5), 2477–2478. https://doi.org/10.1121/1.400986

Cook, N. G. W. (1992). Natural joints in rock: Mechanical, hydraulic and seismic behaviour and properties under normal stress. *International Journal of Rock Mechanics and Mining Sciences*, *29*(3), 198–223. https://doi.org/10.1016/0148-9062(92)93656-5

Hedayat, A., Pyrak-Nolte, L. J., & Bobet, A. (2014). Detection and quantification of slip along non-uniform frictional discontinuities using digital image correlation. *Geotechnical Testing Journal*, *37*(5), 20130141. https://doi.org/10.1520/GTJ20130141

Lin, Q., & Labuz, J. F. (2013). Fracture of sandstone characterized by digital image correlation. *International Journal of Rock Mechanics and Mining Sciences*, *60*, 235–245. https://doi.org/10.1016/j.ijrmms.2012.12.043

Modiriasari, A., Bobet, A., & Pyrak-Nolte, L. J. (2017). Active seismic monitoring of crack initiation, propagation, and coalescence in rock. *Rock Mechanics and Rock Engineering*, *50*(9), 2311–2325. https://doi.org/10.1007/s00603-017-1235-x

Nagata, K., Nakatani, M., & Yoshida, S. (2008). Monitoring frictional strength with acoustic wave transmission. *Geophysical Research Letters*, *35*, L06310. https://doi.org/10.1029/2007GL033146

Nakagawa, S., Nihei, K. T. T., & Myer, L. R. R. (2000). Shear-induced conversion of seismic waves across single fractures. *International Journal of Rock Mechanics and Mining Sciences*, *37*(1-2), 203–218. https://doi.org/10.1016/S1365-1609(99)00101-X

Nolte, D. D., Pyrak-Nolte, L. J., Beachy, J., & Ziegler, C. (2000). Transition from the displacement discontinuity limit to the resonant scattering regime for fracture interface waves. *Rock Mechanics and Rock Engineering*, *37*(1-2), 219–230. https://doi.org/10.1016/S1365-1609(99)00102-1

Pan, B., Qian, K., Xie, H., & Asundi, A. (2009). Two-dimensional digital image correlation for in-plane displacement and strain measurement: A review. *Measurement Science and Technology*, *20*(6), 062001. https://doi.org/10.1088/0957-0233/20/6/062001

Park, C. H., & Bobet, A. (2010). Crack initiation, propagation and coalescence from frictional flaws in uniaxial compression. *Engineering Fracture Mechanics*, *77*(14), 2727–2748. https://doi.org/10.1016/j.engfracmech.2010.06.027

Polikar, R. (1999). The wavelet tutorial. Internet Resources: http://engineering.rowan.edu/polikar/WAVELETS/WTtutorial.html.

Pyrak-Nolte, L. J. (2018). Fracture Specific Stiffness: The critical link between the scaling behavior of hydro-mechanical coupling in fractures and seismic monitoring. In P. Newell & A. Ilgen (Eds.), *Science of carbon storage in deep saline formation, 1st Edition, Process Coupling across Time and Spatial Scales* (pp. 235–253). Amsterdam, Netherlands: Elsevier.

Pyrak-Nolte, L. J., Myer, L. R., & Cook, N. G. W. (1990). Transmission of seismic waves across single natural fractures. *Journal of Geophysical Research*, *95*(B6), 8617. https://doi.org/10.1029/JB095iB06p08617

Pyrak-Nolte, L. J., & Roy, S. (2000). Monitoring fracture evolution with compressional-mode interface waves. *Geophysical Research Letters*, *27*(20), 3397–3400. https://doi.org/10.1029/1999GL011125

Rouet-Leduc, B., Hulbert, C., Lubbers, N., Barros, K., Humphreys, C. J., & Johnson, P. A. (2017). Machine learning predicts laboratory earthquakes. *Geophysical Research Letters*, *44*, 9276–9282. https://doi.org/10.1002/2017GL074677

Schoenberg, M. (1980). Elastic wave behavior across linear slip interfaces. *The Journal of the Acoustical Society of America*, *68*(5), 1516–1521. https://doi.org/10.1121/1.385077

Schoenberg, M. (1983). Reflection of elastic wave from periodically stratified media with interfacial slip. *Geophysical Prospecting*, *31*(2), 265–292. https://doi.org/10.1111/j.1365-2478.1983.tb01054.x

Scuderi, M. M., Marone, C., Tinti, E., Di Stefano, G., & Collettini, C. (2016). Precursory changes in seismic velocity for the spectrum of earthquake failure modes. *Nature Geoscience*, *9*(9), 695–700. https://doi.org/10.1038/ngeo2775

Sheng, Y. (1995). *Wavelet transform, chapter* (p. 10). Boca Raton: CRC and IEEE Press.

Sutton, M. A., Orteu, J. J., & Schreier, H. (2009). *Image correlation for shape, motion and deformation measurements: Basic concepts, theory and applications*. Springer Science & Business Media. Retrieved from https://books.google.com/books?hl=en&lr=&id=AlkqMxpQMLsC&pgis=1